A Multiscale Approach for Modeling Crystalline Solids

A. M. Cuitiño [1], L. Stainier [2], Guofeng Wang [3], Alejandro Strachan [3],

Tahir Çağın[3], William A. Goddard, III [3], and M. Ortiz [4]

[1] Department of Mechanical and Aerospace Engineering

Rutgers University, Piscataway, NJ 08854, USA.

[2] Laboratoire de Techniques Aéronautiques et Spatiales

University of Liège, 4000 Liège, Belgium.

[3] Materials and Process Simulation Center, Beckman Institute (139-74)

California Institute of Technology, Pasadena, CA 91125, USA.

[4] Graduate Aeronautical Laboratories

California Institute of Technology, Pasadena, CA 91125, USA.

November 17, 2017

Abstract

In this paper we present a modeling approach to bridge the atomistic with macroscopic scales in crystalline materials. The methodology combines identification and modeling of the controlling unit processes at microscopic level with the direct atomistic determination of fundamental material properties. These properties are computed using a many body Force Field derived from ab initio quantum-mechanical calculations. This approach is exercised to describe the mechanical response of high-purity Tantalum single crystals, including the effect of temperature and strain-rate on the hardening rate. The resulting atomistically informed model is found to capture salient features of the behavior of these crystals such as: the dependence of the initial yield point on temperature and strain rate; the presence of a marked stage I of easy glide, specially at low temperatures and high strain rates; the sharp onset of stage II hardening and its tendency to shift towards lower strains, and eventually disappear, as the temperature increases or the strain rate decreases; the parabolic stage II hardening at low strain rates or high temperatures; the stage II softening at high strain rates or low temperatures; the trend towards saturation at high strains; the temperature and strain-rate dependence of the saturation stress; and the orientation dependence of the hardening rate.

1

1   Introduction

This paper is concerned with the development of a multiscale modeling approach for advanced materials such as high-purity bcc single crystals. The present approach is aligned with the current *divide and conquer* paradigm in micromechanics (see, e. g., [1, 2, 3, 4, 5, 6]. This paradigm first identifies and models the controlling unit process at microscopic scale. Then, the energetics and dynamics of these mechanisms are quantified by means of atomistic modeling. Finally, the macroscopic driving force is correlated to macroscopic response via microscopic modeling. This last step involves two stages, *localization* of the macroscopic driving force into unit-process driving forces and *averaging* of the contribution of each unit process into the macroscopic response.

We show in this article that the meticulous application of this paradigm renders truly predictive models of the mechanical behavior of complex systems. In particular we predict the hardening of Ta single crystal and its dependency for a wide range of temperatures and strain rates. The feat of this approach is that predictions from these atomistically informed models recover most of the macroscopic characteristic features of the available experimental data, without a priori knowledge of such experimental tests. This approach then provides a procedure to forecast the mechanical behavior of material in extreme conditions where experimental data is simply not available or very difficult to collect.

A crucial step in this approach is the appropriate selection and modeling of the unit processes. These models supply the link between the atomic and meso scale by identifying and correlating the relevant material properties, susceptible of atomistic determination such as energy formation for defects, with the corresponding driving forces. In this case, we specifically consider the following unit processes: double-kink formation and thermally activated motion of kinks; the close-range interactions between primary and forest dislocation, leading to the formation of jogs; the percolation motion of dislocations through a random array of forest dislocations introducing short-range obstacles of different strengths; dislocation multiplication due to breeding by double cross-slip; and dislocation pair-annihilation.

A set of material parameters is then obtained from the modeling and identification stage, which is required to quantify the contribution of each of the unit processes. We compute these materials properties using a combination of ab-initio quantum mechanics (QM) and Force Field (FF) calculations. QM describes the atomic interactions from first principles, i.e. with no input from experiments; unfortunatelly QM methods are computationally intensive and restricted to small systems, making QM calculations impractical to study most of the materials properties governing plasticity. Force Fields give the total energy of a system as a potential energy function of the atomic positions and with Molecular Dynamics (MD) allows the simulation of systems containing millions of atoms. We used ab-initio quantum mechanical calculations (equations of state of various crystalline phases, elastic constants, energetics of defects, etc.) to develop a many body Force Field (FF) (named qEAM FF) for Tantalum. We use the qEAM FF with MD to calculate the core energy of the $1/2a < 111 >$ screw dislocation, that of the edge dislocation with Burgers vector $b = 1/2a < 111 >$ in (110) planes. We have also calculated the formation energies and nucleation lengths of the kinks in $b = 1/2a < 111 >$ screw dislocations.

The organization of the paper follows the sequential stages of the proposed approach. First, we provide a brief description of each of the unit processes including the governing final equations. We then identify and compute by atomistic means the corresponding material properties. Finally,
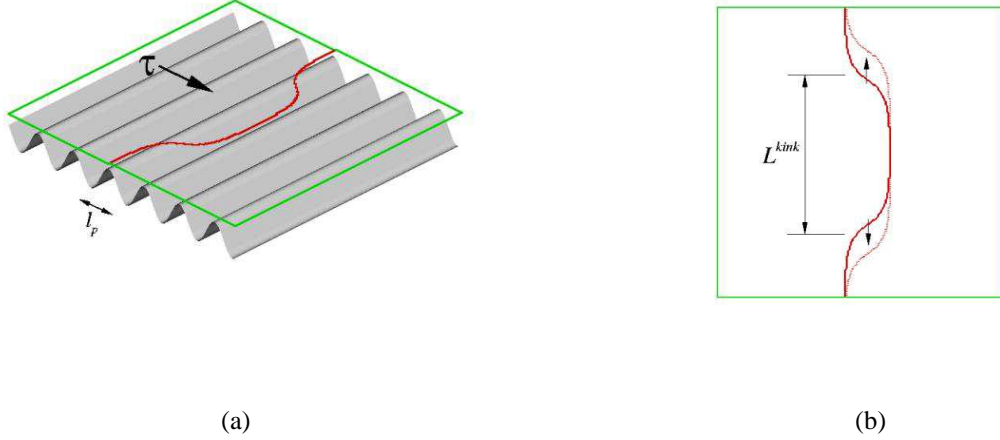
(a)   (b)

Figure 1: Schematic of the double-kink mechanism.

we compare the predictions against experimental data.

2   Unit Processes

Plastic deformation in metallic systems is the macroscopic manifestation of dislocation activity. The resistance to the dislocation motion, therefore, engenders the hardening properties observed in this type of materials. It is then the complex interplay of microscopic mechanisms control-ling **dislocation mobility, dislocation interaction and dislocation evolution** which confers the macroscopic constitutive properties. In the present approach, these controlling processes are con-sidered to be *orthogonal* in the sense that are weakly coupled with each other. The interaction among them is only established through the uniqueness of the macroscopic driving force which are shared, via the localization process, by all the unit processes.

In this section, we introduce the set of controlling unit processes which have been identified for describing the mechanical response of high-purity BCC single crystals, in particular for Tantalum. We also provide the final expression resulting from the the modeling of each of these processes. A detailed description of the model, including comparison with experimental data is given in [7].

2.1   Dislocation Mobility: Double-Kink Formation and Thermally Activated Motion of Kinks

We consider the thermally activated motion of dislocations within an *obstacle-free* slip plane. Un-der these conditions, the motion of the dislocations is driven by an applied resolved shear stress τ and is hindered by the lattice resistance, which is weak enough that it may be overcome by thermal activation. The lattice resistance is presumed to be well-described by a Peierls energy function,
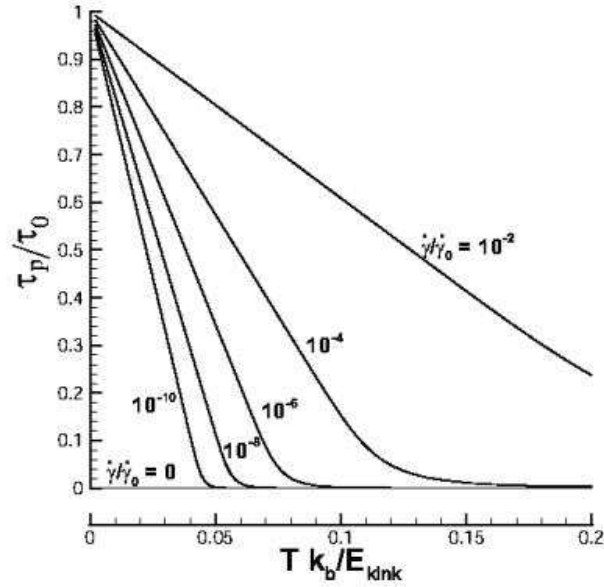
3

Figure 2: Temperature dependence of the effective Peierls stress for various strain rates. Note that the typical order of magnitude of $\dot{\gamma}_0^{\text{kink}} = 10^6 \ s^{-1}$.

which assigns an energy per unit length to dislocation segments as a function of their position on the slip plane.

In bcc crystals, the core of screw dislocation segments relaxes into low-energy non-planar configurations [8, 9, 10, 11, 12, 5, 13, 14]. This introduces deep valleys into the Peierls energy function aligned with the Burgers vector directions and possessing the periodicity of the lattice. At low temperatures, the dislocations tend to adopt low-energy configurations and, consequently, the dislocation population predominantly consists of long screw segments. In order to move a screw segment normal to itself, the dislocation core must first be constricted, which requires a substantial supply of energy. Thus, the energy barrier for the motion of screw segments, and the attendant Peierls stress, may be expected to be large, and the energy barrier for the motion of edge segments to be comparatively smaller. For instance, Duesbery and Xu [15] have calculated the Peierls stress for a rigid screw dislocation in Mo to be 0.022μ, where μ is the $\langle 111 \rangle$ shear modulus, whereas the corresponding Peierls stress for a rigid edge dislocation is 0.006μ, or about one fourth of the screw value. This suggests that the rate-limiting mechanism for dislocation motion is the thermally activated motion of kinks along screw segments ([16, 17, 18]).

At sufficiently high temperatures and under the application of a resolved shear stress $\tau > 0$, a double-kink may be nucleated with the assistance of thermal activation (e. g., [19, 20, 5], and the subsequent motion of the kinks causes the screw segment to effectively move forward, Fig. 1. Under this conditions the following expression for the effective temperature and strain-rate
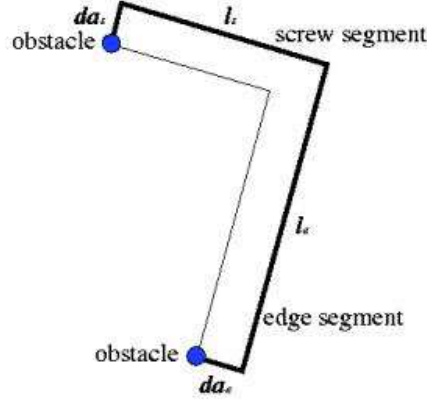
4

Figure 3: Bow-out mechanism for a dislocation segment bypassing an obstacle pair

dependent Peierls τ_p is obtained:

$$\tau_P = \frac{\tau_0}{\beta E^{\text{kink}}} \text{asinh} \left(\frac{\dot{\gamma}}{\dot{\gamma}_0^{\text{kink}}} e^{\beta E^{\text{kink}}} \right) \tag{1}$$

where the effective Peierls stress is given by

$$\tau_0 = \frac{E^{\text{kink}}}{bL^{\text{kink}}l_P} \tag{2}$$

and the reference strain is defined as

$$\dot{\gamma}_0^{\text{kink}} = 2b\rho l_P \nu_D \tag{3}$$

In the preceeding equations, b is the Burgers vector, ρ is the dislocation density, $\beta = 1/k_B T$, k_B is Boltzmann's constant, T is the absolute temperature, and ν_D is the attempt frequency which may be identified with the Debye frequency to a first approximation. Also, l_P is the distance between two consecutive Peierls valleys. For bcc crystals, $l_P = \sqrt{2/3}a$ if the slip plane is $\{110\}$, $l_P = \sqrt{2}a$, if the slip plane is $\{112\}$, and $l_P = \sqrt{8/3}a$ if the slip plane is $\{123\}$, where a is the cubic lattice size [21]. Finally, E^{kink} is the energy of formation of a kink-pair and L^{kink} is the length of an incipient double kink. The formation energy E^{kink} and the length L^{kink}, which cannot be reliably estimated from elasticity since the energy is composed mostly of core region, can, however, be accurately computed by recourse to atomistic models as shown in section 3. Modeling of this first unit process renders the first 2 material properties amenable of atomistic calculations.

In Figure 2 the dependence of the effective Peierls stress on temperature and rate of deformation is illustrated. The Peierls stress decreases ostensibly linearly up to a critical temperature T_c, beyond which it tends to zero. These trends are in agreement with the experimental observations
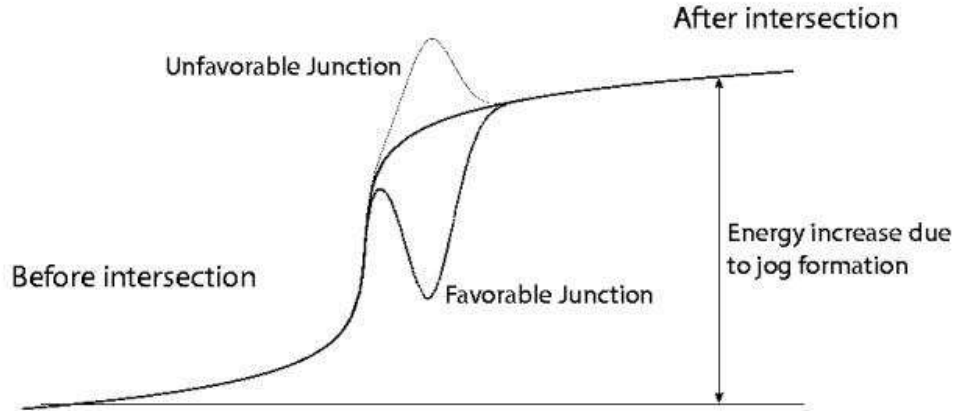
Figure 4: Schematic of energy variation as a function of a reaction coordinate during dislocation intersection and crossing.

of Wasserbäch [22] and Lachenmann and Schultz [23]. The critical temperature T_c increases with the strain rate. In particular, in this model the effect of increasing (decreasing) the strain rate has an analogous effect to decreasing (increasing) the temperature, and vice-versa, as noted by Tang *et al.* [24]. In the regime of very high strain-rates ($\dot{\gamma} > 10^5 \ s^{-1}$), effects such as electron and phonon drag become important and control the velocity of dislocations [25, 26].

2.2 Dislocation Interactions: Obctacle-Pair Strength and Obstacle Strength

In the forest-dislocation theory of hardening, the motion of dislocations, which are the agents of plastic deformation in crystals, is impeded by secondary –or 'forest'– dislocations crossing the slip plane. As the moving and forest dislocations intersect, they form jogs or junctions of varying strengths [27, 28, 4, 29, 30, 31, 32, 33, 34] which, provided the junction is sufficiently short, may be idealized as point obstacles. Moving dislocations are pinned down by the forest dislocations and require a certain elevation of the applied resolved shear stress in order to bow out and bypass the pinning obstacles. For the case of infinitely strong obstacles, the resistance of the forest is provided by the strength of the obstacle pairs. This obstacle pair strength is subsequently reduced by considering that point obstacles composing the pair can only provide a finite strength. The processes imparting the pair-obstacle strength and obstacle strength are described next

2.2.1 Obstacle-Pair Strength

We begin by treating the case of infinitely strong obstacles. In this case, pairs of obstacles pin down dislocation segments, which require a certain threshold resolved shear stress s in order to overcome the obstacle pair. The lowest-energy configuration of unstressed dislocation segments spanning an
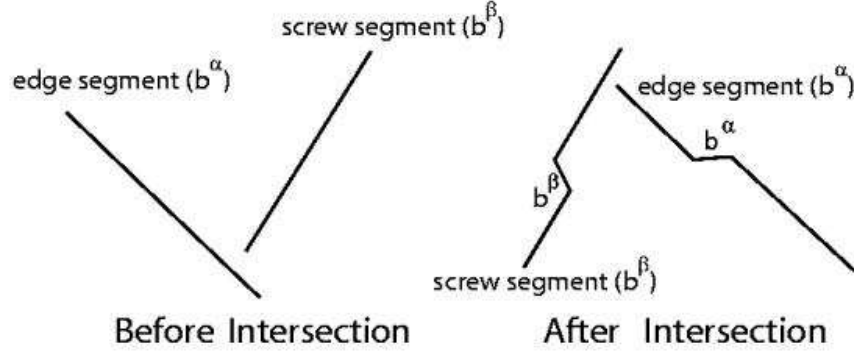
6

Figure 5: Schematic of jog formation during dislocation intersection

obstacle pair is a step of the form shown as the thin line in Fig. 3. Under these conditions, the bow-out mechanism by which a dislocation segment bypasses an obstacle pair may be expected to result in the configuration shown in Fig. 3 (bold line). If the edge-segment length is l_e, a displacement da_e of the dislocation requires a supply of energy equal to $2U^{\text{screw}}da_e + b\tau_P^{\text{edge}}l_e da_e$ in order to overcome the Peierls resistance τ_P^{edge} and to extend the screw segments. The corresponding energy release is $b\tau l_e da_e$. Similar contributions result from a displacement da_s of the screw-segment of length l_s. Retaining dominant terms the obstacle-pair strength is

$$s = \tau_P^{\text{screw}} + \frac{2U^{\text{edge}}}{bl_s} \tag{4}$$

The obstacle-pair strength can be therefore estimated by quantifying τ_P, l_s and U^{edge}. An expression for the Peierls stress τ_P is given in Eq. (1), the distance between obstacles along the screw direction l_s is estimated by statistics assuming a random obstacle distribution and the core energy per unit length in the edge direction U^{edge} is obtained by atomistic calculations presented in the following sections.

2.2.2 Obstacle Strength

In this section we proceed to estimate the obstacle strengths which reduces the obstacle-pair strength described in the previuos section. The interaction between primary and secondary dislocations may result in a variety of reaction products, including jogs and junctions [30, 31, 27, 32, 24, 28, 4, 34, 29]. Experimental estimates of junction strengths have been given by Franciosi and Zaoui [35] for the twelve slip systems belonging to the family of {111} planes and [110] directions in fcc crystals, and by Franciosi [36] for the twenty-four systems of types {211} [111] and {110} [111] in bcc crystals. The strength of some of these interactions has recently been computed using atomistic and continuum models [27, 28, 4, 29]. Tang *et al.* have numerically estimated the average strength of dislocation junctions for Nb and Ta crystals [24].

For purposes of the present theory, we specifically concern ourselves with short-range interactions between dislocations which can be idealized as point defects. For simplicity, we consider the
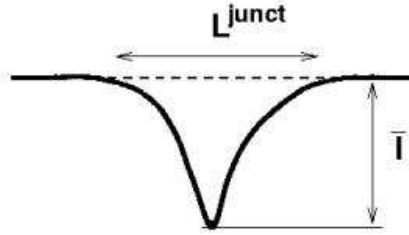
7

Figure 6: Schematic of a dislocation line overcoming a junction

case in which each intersecting dislocation acquires a jog. The energy of a pair of crossing disloca-
tions is schematically shown in Fig. 4 as a function of some convenient reaction coordinate, such
as the distance between the dislocations. The interaction may be repulsive, resulting in an energy
barrier, or attractive, resulting in a binding energy, Fig. 4. In the spirit of an equilibrium theory,
here we consider only the final reaction product, corresponding to a pair of jogged dislocations
at infinite distance from each other, and neglect the intermediate states along the reaction path.
In addition, we deduce the strength of the obstacles directly from the energy supply required to
attain the final state, i. e. the jog-formation energy. Despite the sweeping nature of these assump-
tions, the predicted saturation strengths in multiple slip are in good agreement with experiment (cf
Section 4), which lends some empirical support to the theory.

   We estimate the jog formation energy as follows. Based on energy and mobility considerations
already discussed, we may expect the preponderance of forest dislocations to be of screw character,
and the mobile dislocation segments to be predominantly of edge character. We therefore restrict
our analysis to intersections between screw and edge segments. The geometry of the crossing
process is schematically shown in Fig. 5. Each dislocation acquires a jog equal to the Burgers
vector of the remaining dislocation. The energy expended in the formation of the jogs may be
estimated as

$$
E^{jogs}_{\alpha\beta} \sim \begin{cases} bU^{\mathrm{screw}} \left[1 - r\cos\theta^{\alpha\beta}\right] & \text{if } \mathbf{b}^{\alpha} = \mathbf{b}^{\beta} \\ bU^{\mathrm{screw}} \left[2r - \cos(\theta^{\beta\alpha}) - r\cos\theta^{\alpha\beta}\right] & \text{otherwise} \end{cases}
\tag{5}
$$

where $r = U^{\mathrm{edge}}/U^{\mathrm{screw}}$ is the ratio of screw to edge dislocation line energies. This ratio is
computed by atomistic calculations presented in the next section, renders a value of $r = 1.77$ for
Ta. The resulting jog formation energies for the complete collection of pairs of $\{211\}$ and $\{110\}$
dislocations are tabulated in Table 1.

   A derivation entirely analogous to that leading to Eq. (1) yields the following expression for
the strength of an obstacle in the slip system α produced by a forest segment in the system β

$$
s^{\alpha\beta} = \frac{s_0^{\alpha\beta}}{\beta E^{\mathrm{jog}}_{\alpha\beta}} \mathrm{asinh} \left(\frac{\dot{\gamma}^{\alpha}}{\dot{\gamma}_0^{\alpha}} e^{\beta E^{\mathrm{jog}}_{\alpha\beta}} \right)
\tag{6}
$$

8

	A2	A2'	A3	A3'	A6	A6'	B2	B2"	B4	B4'	B5	B5'	C1	C1'	C3	C3"	C5	C5"	D1	D1"	D4	D4"	D6	D6"
A2	—-	1.0	1.0	1.0	1.0	1.0	1.5	1.5	1.5	1.5	1.5	1.5	2.4	2.4	2.4	2.4	2.4	2.4	2.4	2.4	2.4	2.4	2.4	2.4
A2'	1.0	—-	1.0	1.0	1.0	1.0	3.2	3.2	3.2	3.2	3.2	3.2	1.8	1.8	1.8	1.8	1.8	1.8	1.8	1.8	1.8	1.8	1.8	1.8
A3	1.0	1.0	—-	1.0	1.0	1.0	2.4	2.4	2.4	2.4	2.4	2.4	1.5	1.5	1.5	1.5	1.5	1.5	2.4	2.4	2.4	2.4	2.4	2.4
A3'	1.0	1.0	1.0	—-	1.0	1.0	1.8	1.8	1.8	1.8	1.8	1.8	3.2	3.2	3.2	3.2	3.2	3.2	1.8	1.8	1.8	1.8	1.8	1.8
A6	1.0	1.0	1.0	1.0	—-	1.0	2.4	2.4	2.4	2.4	2.4	2.4	2.4	2.4	2.4	2.4	2.4	2.4	1.5	1.5	1.5	1.5	1.5	1.5
A6'	1.0	1.0	1.0	1.0	1.0	—-	1.8	1.8	1.8	1.8	1.8	1.8	1.8	1.8	1.8	1.8	1.8	1.8	3.2	3.2	3.2	3.2	3.2	3.2
B2	1.5	1.5	1.5	1.5	1.5	1.5	—-	1.0	1.0	1.0	1.0	1.0	2.4	2.4	2.4	2.4	2.4	2.4	2.4	2.4	2.4	2.4	2.4	2.4
B2"	3.2	3.2	3.2	3.2	3.2	3.2	1.0	—-	1.0	1.0	1.0	1.0	1.8	1.8	1.8	1.8	1.8	1.8	1.8	1.8	1.8	1.8	1.8	1.8
B4	2.4	2.4	2.4	2.4	2.4	2.4	1.0	1.0	—-	1.0	1.0	1.0	2.4	2.4	2.4	2.4	2.4	2.4	1.5	1.5	1.5	1.5	1.5	1.5
B4'	1.8	1.8	1.8	1.8	1.8	1.8	1.0	1.0	1.0	—-	1.0	1.0	1.8	1.8	1.8	1.8	1.8	1.8	3.2	3.2	3.2	3.2	3.2	3.2
B5	2.4	2.4	2.4	2.4	2.4	2.4	1.0	1.0	1.0	1.0	—-	1.0	1.5	1.5	1.5	1.5	1.5	1.5	2.4	2.4	2.4	2.4	2.4	2.4
B5'	1.8	1.8	1.8	1.8	1.8	1.8	1.0	1.0	1.0	1.0	1.0	—-	3.2	3.2	3.2	3.2	3.2	3.2	1.8	1.8	1.8	1.8	1.8	1.8
C1	1.8	1.8	1.8	1.8	1.8	1.8	1.8	1.8	1.8	1.8	1.8	1.8	—-	1.0	1.0	1.0	1.0	1.0	3.2	3.2	3.2	3.2	3.2	3.2
C1'	1.8	1.8	1.8	1.8	1.8	1.8	1.8	1.8	1.8	1.8	1.8	1.8	1.0	—-	1.0	1.0	1.0	1.0	3.2	3.2	3.2	3.2	3.2	3.2
C3	1.5	1.5	1.5	1.5	1.5	1.5	2.4	2.4	2.4	2.4	2.4	2.4	1.0	1.0	—-	1.0	1.0	1.0	2.4	2.4	2.4	2.4	2.4	2.4
C3"	3.2	3.2	3.2	3.2	3.2	3.2	1.8	1.8	1.8	1.8	1.8	1.8	1.0	1.0	1.0	—-	1.0	1.0	1.8	1.8	1.8	1.8	1.8	1.8
C5	2.4	2.4	2.4	2.4	2.4	2.4	1.5	1.5	1.5	1.5	1.5	1.5	1.0	1.0	1.0	1.0	—-	1.0	2.4	2.4	2.4	2.4	2.4	2.4
C5"	1.8	1.8	1.8	1.8	1.8	1.8	3.2	3.2	3.2	3.2	3.2	3.2	1.0	1.0	1.0	1.0	1.0	—-	1.8	1.8	1.8	1.8	1.8	1.8
D1	1.8	1.8	1.8	1.8	1.8	1.8	1.8	1.8	1.8	1.8	1.8	1.8	3.2	3.2	3.2	3.2	3.2	3.2	—-	1.0	1.0	1.0	1.0	1.0
D1"	1.8	1.8	1.8	1.8	1.8	1.8	1.8	1.8	1.8	1.8	1.8	1.8	3.2	3.2	3.2	3.2	3.2	3.2	1.0	—-	1.0	1.0	1.0	1.0
D4	2.4	2.4	2.4	2.4	2.4	2.4	1.5	1.5	1.5	1.5	1.5	1.5	2.4	2.4	2.4	2.4	2.4	2.4	1.0	1.0	—-	1.0	1.0	1.0
D4"	1.8	1.8	1.8	1.8	1.8	1.8	3.2	3.2	3.2	3.2	3.2	3.2	1.8	1.8	1.8	1.8	1.8	1.8	1.0	1.0	1.0	—-	1.0	1.0
D6	1.5	1.5	1.5	1.5	1.5	1.5	2.4	2.4	2.4	2.4	2.4	2.4	2.4	2.4	2.4	2.4	2.4	2.4	1.0	1.0	1.0	1.0	—-	1.0
D6"	3.2	3.2	3.2	3.2	3.2	3.2	1.8	1.8	1.8	1.8	1.8	1.8	1.8	1.8	1.8	1.8	1.8	1.8	1.0	1.0	1.0	1.0	1.0	—-

Table 1: Normalized jog-formation energies resulting from crossings of bcc dislocations.

where the strength at zero temperature is given by

$$s_0^{\alpha\beta} = \frac{E_{\alpha\beta}^{\text{jog}}}{b\bar{l}^\alpha L^{\text{junct}}} \tag{7}$$

and the reference strain rate by

$$\dot{\gamma}_0^\alpha = 2\rho^\alpha b\bar{l}^\alpha \nu_D \tag{8}$$

The lengths $\bar{l}^\alpha$ and L^{junct} describe the geometry of the junction as illustrated in Fig. (6). These values, which have been estimated to be of the order of few b in the present case, can also be obtained by atomistic models.

2.3 Dislocation Evolution: Multiplication and Attrition

The density of forest obstacles depends directly on the dislocation densities in all slip systems of the crystal. Therefore, in order to close the model we require a equation of evolution for the dislocation densities. Processes resulting in changes in dislocation density include production by fixed sources, such as Frank-Read sources, breeding by double cross slip and pair annihilation (see [37] for a review; see also [38, 39, 40, 41, 42, 43]). Although the operation of fixed Frank-Read sources is quickly eclipsed by production due to cross slip at finite temperatures, it is an important mechanisms at low temperatures. The double cross-slip, fixed Frank-Read sources and pair annihilation mechanisms are next considered in turn.

2.3.1 Dislocation Multiplication: Fixed Frank-Reed and Breeding by Cross Glide

The rate of dislocation multiplication in a given slip system α produced by fixed Frank-Reed sources and by breeding by cross glide is written as

$$b\dot{\rho}^\alpha = \lambda_0 \sqrt{\rho^\alpha} \dot{\gamma}^\alpha \tag{9}$$

where λ_0 is a constant associated with the fixed Frank-Read production; this parameter is rather topological than material dependent.

2.3.2 Attrition: Pair Annihilation

The rate of dislocation attrition due to pair annihilation may finally be estimated as:

$$b\dot{\rho}^\alpha = -\kappa\rho^\alpha \dot{\gamma}^\alpha \tag{10}$$

where κ is the effective annihilation distance. This is the maximum distance at which two screw segments with opposite direction and forced to move with a velocity $v = \dot{\gamma}/b\rho$ will annihilate. This distance can be estimated by simply equating the time required for trapping and escaping. Trapping is governed by the elastic interaction forces (attraction) while escaping by the applied strain rate. Then,

$$\frac{1}{\kappa} = \frac{1}{\kappa_c} + \frac{1}{\kappa_0 \left(A + \sqrt{A^2 + 1}\right)} \tag{11}$$

where

$$A = \mathrm{e}^{-\beta E^{\mathrm{jog}}} \beta E^{\mathrm{jog}} \dot{\gamma}_0^{\mathrm{jog}} / \dot{\gamma}^{\alpha} \tag{12}$$

is a factor depending on the strain rate and temperature,

$$\dot{\gamma}_0^{\mathrm{jog}} = 2b\rho l_P \nu_D \tag{13}$$

is a reference slip-strain rate and κ_c is the cut-off value corresponding the effective screening distance. It follows that the critical pair-annihilation distance κ decreases with increasing strain rate and decreasing temperature. Thus, at high strain rates the dislocation velocities are high and the probability of being captured by another dislocation diminishes accordingly. Additionally, an increase in temperature increases the dislocation mobility and speeds up the annihilation process, which results in an attendant increase in annihilation rates. The rate of annihilation is then modulated by the nucleation energy of a jog E^{jog} which can be calculated from atomistic simulations.

3 Atomistic modeling of dislocations properties

In the previous section we have identified the following set of *material parameters* required to estimate the contribution of each of the controlling unit processes: E^{kink}, L^{kink}, U^{edge} U^{screw}, and E^{jog}. In this section we briefly describe the computation of them using a First Principles-based Force Field with Molecular Dynamics.

Quantum mechanics (QM) describes the atomic interactions from first principles, i.e. using no empirical input. Unfortunately QM methods are computationaly intensive and thus only applicable to small systems (hundreds of atoms) and short times (picoseconds). The study of most of the unit processes that govern the plasticity of materials (such as dislocation mobility, kink energies, etc.) involve many atoms and long simulation times. Such problems require the use of Force Fields, where the total energy of the system is given by a potential energy function of the atomic positions and does not involve the solution of Shrodinger's equation. The drawback of using potentials to describe the atomic interactions is that some accuracy is lost; it is thus of great importance to use accurate force fields to describe the atomic interactions.

We developed a many body Force Field for Tantalum based on accurate QM calculations [44] which can be used with Molecular Dynamics (MD) to simulate systems containing millions of atoms. We fitted an Embedded Atom Model type Force Field (named qEAM FF) to a variety of ab initio calculations, including the zero temperature Equation of State (EOS) for bcc, fcc, and A15 phases of Ta in a wide pressure range, elastic constants, vacancy formation energy and energetics of a shear transformation in the twinning direction [44]. Ta is a bcc metal and no phase transition to other crustalline phase is known, but using QM we can calculate the EOS of thermodynamicaly unstable or metastable phases (such as A15, fcc, hcp, etc.). Including data about these high energy phases, with different coordination numbers, in the Force Field training set is important to correctly describe the atomic interactions near defects such as dislocations, grain boundaries, etc.

We have used the qEAM with MD to study a variety of materials properties such as the melting temperature of Ta as a function of pressure [44], dislocation properties [14], and spall failure [45].

In subsection 3.1 we show the calculation of the core energy of edge and screw dislocations in Ta and in Subsection 3.2 we calculate the double kink formation energy and nucleation length.
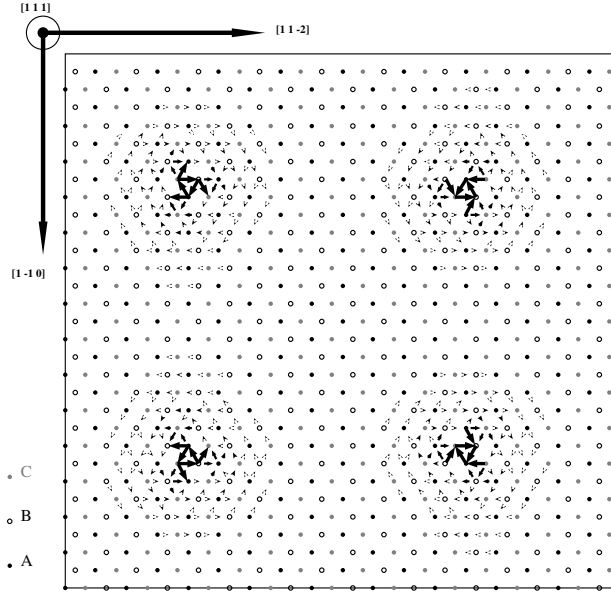
Figure 7: Differential displacement map of a relaxed quadrupole of screw dislocation in Ta.

3.1 Core energy of the $1/2a < 111 >$ screw and edge dislocations

In order to study static properties of the 1/2a< 111 > screw dislocation in Ta such us core structure and energy we use a dislocation quadrupole in a simulation cell with periodic boundary conditions. Two of the dislocations have Burgers vector b=1/2a< 111 > and the other two have b=-1/2a< −1−1−1 >. Such an arrangement of dislocations minimizes the misfit of atoms on the periodic boundary due to the effects of periodic images. We build the dislocations using the atomic displacements obtained from elasticity theory and then we relax the atomic coordinates using the qEAM FF. In the bcc structure, there are two kinds of dislocation core configurations (easy core and hard core) that can be transformed to each other by reversing the Burgers vector [11]. In this work we focus on the lower energy easy cores. In Figure 7 we show the differential displacement map (DDM) of our relaxed quadrupolar system. In the DDM atoms are represented by circles and projected on a (111) plane. The arrows represent the relative displacement in [111] direction of neighboring atoms due to the dislocation. We can see from Figure 7 that the equilibrium dislocation core obtained using qEAM FF has three-fold symmetry and spreads out in three < 112 > directions on 110 planes.

Lets define strain energy as the total energy of our system once the perfect crystal energy is subtracted. The total strain energy can be divided in two terms: core energy (E_c) and elastic energy (E_e). The latter contains the self-energy of each dislocation and their interactions and can be calculated using linear elasticity theory. The core energy is the energy contained close to the dislocation line (closer than some distance r_c called core radius) where, due to the large strain, elasticity theory is not valid and the details of the interatomic interactions are important. For our
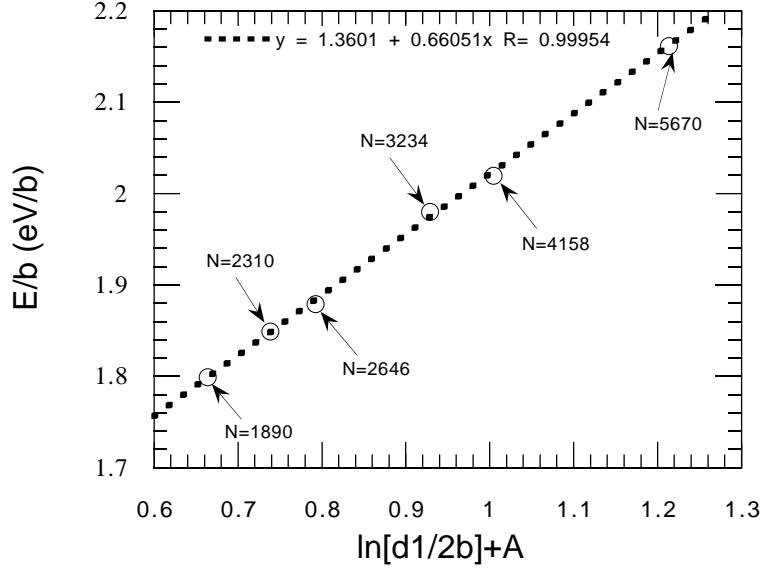
Figure 8: Total strain energy of the quadrupolar system as a function of $\ln d_1/r_c + A(d_1/d_2)$; the number of atoms in each simulation is shown. The dashed line is the linear fit to our atomistic data.

quadrupole system the total strain energy takes the form [13]:

$$E = E_c(r_c) = Kb^3 \left[\ln \frac{d_1}{r_c} + A\left(\frac{d_1}{d_2}\right) \right], \tag{14}$$

where K depends on the elastic constants, d_1 and d_2 are the nearest separation of dislocations along $< 11 - 2 >$ and $< 1 - 10 >$ directions and $A(d_1/d_2)$ is a geometric factor which comes from the dislocation interactions.

    We studied quadrupolar dislocation cells of different sizes. In Figure (8) we show the minimized energy as a function of $\ln d_1/r_c + A(d_1/d_2)$ for the different simulation cells; in order to compare with previous calculations [11, 13] we took $r_c = 2b$. We can see that the total energies follow a straight line as predicted by elasticity theory (Eq. 14), showing that the value chosen for the core radius is large enough to take account for the non elastic region near the dislocation line. From a linear fit to our data we determine the core energy $E_c = 1.30$ eV/b and $K = 3.33 \times 10^{-2} eV/A3$. The value of K can also be computed from the elastic constants giving $3.33 \times 10^{-2} eV/A3$ in excellent agreement with the one obtained from the fit. Recent ab initio calculations of core energy (using periodic cells containing 90 atoms) give 0.86 eV/b, lower than the value obtained with qEAM FF and the dislocation cores are compact and symmetric [13].

    Using the qEAM we can calculate the strain energy associated with each atom. In Figure (9) we show the atomic energy distribution (number of atoms per dislocation per Burgers vector as a function of their strain energy) for a system containing 5670 atoms in the periodic cell. We can see that there are 6 atoms with atomic strain energy higher than 0.15 eV and another 6 atoms with energy in the range 0.06-0.08 eV. They correspond to the 12 atoms per dislocation per Burgers

13
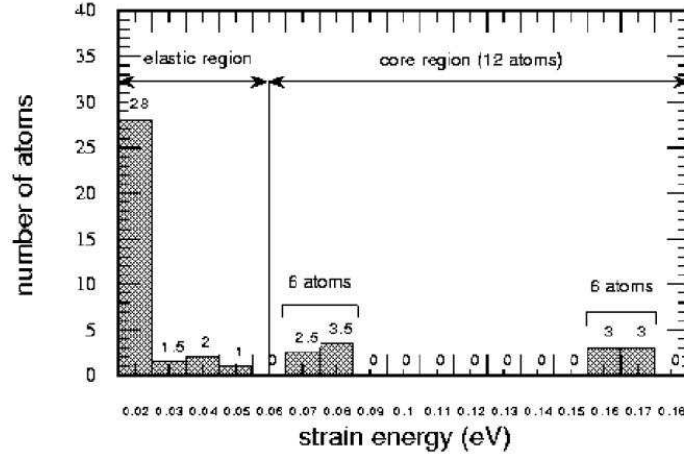
Figure 9: Histogram of atomistic strain energy distribution for the quadrupolar arrangement of screw dislocations. The cell contains 5670 atoms and is 7 Burgers vectors long.

vector closer to the dislocation line and their total energy is 1.35eV/b, very similar the core energy obtained from Eq. 14. The rest of the atoms have lower strain energy and can be cosidered as the elastic part of the system. We can then define the dislocation core as formed by the 12 atoms per Burgers vector with higher energy.

We have also calculated the core energy of the edge dislocation with $b = 1/2a < 111 >$ on a (110) plane. We build a simulation cell with axis oriented along $< 112 >$ (x axis), $< 110 >$ (y axis), and $1/2a < 111 >$ (z axis); this cell contains 6 atoms. We then replicate the cell 3 times along x, 16 times along y, and 20 times along z; the number of atoms in the cell is then N=5760. We then remove 108 atoms to form a dipole of edge dislocations. Once the system is relaxed (both atoms and cell parameters) we have a $24.3967\text{Å} \times 75.1824\text{Å} \times 56.632$ Åcell. Figure (10) shows a snapshot of the atoms projected on a $< 112 >$ plane.

In Figure 11 we show the energy distribution for the edge dislocation (number of atoms per dislocation and per $a < 112 >$ length as a function of their energy). Figure 11 shows that the core of the edge dislocation contains atoms with higher energies and a broader distribution of energies as compared with the screw case [Figure (9)]. Taking into accound Figure 11 we define the core of the edge dislocation as formed by those atoms with strain energy higher that 0.1 eV. This definition leads to 36 atoms per $a < 112 >$ or ~ 4.42 atoms per Å and to a core energy of $E_{core}^{edge} = 0.827$ eV/Å(in the case of the screw we had 12 atoms/b or ~ 4.17 atoms per Å). The ratio between the core energy of the edge and that of the screw is: $E_{core}^{edge}/E_{core}^{screw} \sim 1.77$. It is important to mention that changing the number of atoms considered to belong to the core changes the core energy, but the difference is minor. Had we taken the 34 atoms per $a < 112 >$ with higher energy as the core (leading to ~ 4.18 atoms /Å, a density very similar to the one obtained in the screw dislocation) we get a very similar core energy: $E_{core}^{edge} = 0.80$ eV/Å.

14

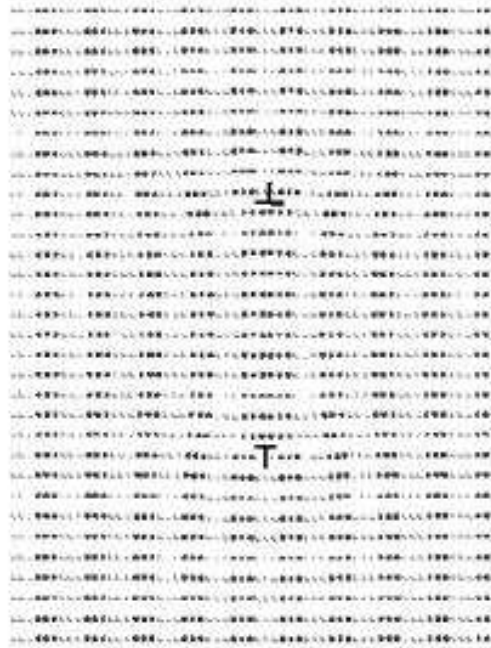Edge dislocations in Ta
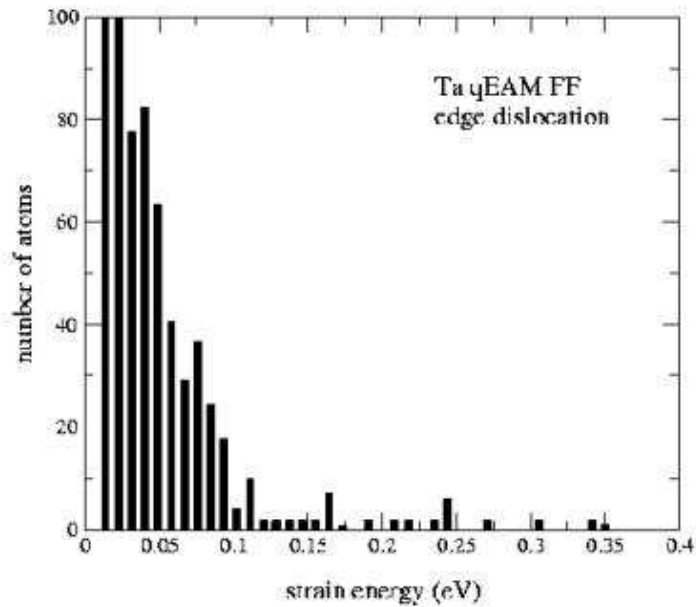
strain energy (eV)

Figure 11: Histogram of atomistic strain energy distribution for the dipole of edge dislocations. The number of atoms is given per dislocation and per $1/2a < 112 >$ length.

15

3.2 Kink pair energy and nucleation lenght

As already explained the kink pair mechanism controls the mobility of screw dislocations in bcc metals and atomistic simulations can provide the details of this mechanism.

As we can see from Figure (7) the core of the screw dislocation spreads in three $< 112 >$ directions, this leads to two distint, but energetically equilavent, core configurations; we will name them positive (P) and negative (N) cores [46]. The shorter (and lower energy) kinks possible involves the displacement of the position of the dislocation line in the (111) plane from one equilibrium position to a nearest neighbor equilibrium position; the displacement involved is $1/3a < 112 >$. There are six possible $< 112 >$ directions but only two need to be considered by symmetry, this leads to two kink directions which we will call left (L) and right (R). The two dislocation cores (N and P) and two directions (L and R) lead to 8 different single kinks: NRP, NRN, PRP, PRN, NLP, NLN, PLP and PLN. We have studied all of them in detail [46], here we will concentrate on the single kinks that lead to the lowest energy kink pair. We calculated the formation energy and length of the various kinks using quadrupolar arrangements of dislocations as explained in subsection 3.1. The simulation cell lengths are 40.7 Å in the [11-2] direction, 42.3 Å in [1-10] and 431.8 Å in [111] containing 40500 atoms; the details of these calculations can be found in [46]. We calculate the kink energy as the difference of strain energy between the quadrupolar systems containing kinks and that corresponding to perfect straight dislocations. This energy difference is divided by four to get the energy per kink. Using the qEAM FF we find that the lowest energy kink pair is formed combining the PLN and NRP kinks. We define the kink pair nucleation energy as the sum of the formation energy of the two songle kinks leading to $E^{kink} = 0.725$ eV. The nucleation energy calculated in this way does not take into account the attractive interaction between the two kinks which lowerers the nucleation energy. This interation energy is very small for separation larger than ~ 15 b [11, 20].

As explained above, a critical parameter for the micro-mechanical modeling of plasticity is, apart from the kink pair energy, its nucleation length L_{kink}. We studied both the energetics and structure of the variuos kinks along the dislocation line. Figure 12 shows the extent of the kinks both from structural and energetic points of view. We show the position of the dislocation in the direction of the kink along the dislocation line for a PLN kink [Figure 12(a)] and NRP kink [Figure 12(c)]. We also show the total energy of the quadrupolar system along the dislocation line for the PLN [Figure 12(b)] and NRP [Figure 12(d)] kinks. This is calculated by dividing the system in the [111] direction in regions of width equal to the Burgers vector and calculating the total energy in each slice. The structural length of the PLN kinks is $L_{str}^{PLN} = 8$ b [Figure 12 (a)]; while its "energetic extent" is $L_{ene}^{PLN} = 14$ b [Figure 12 (b)]. For NRP kinks we obtain: $L_{str}^{NRP} = 8$ b [Figure 12 (c)] and $L_{ene}^{NRP} = 20$ b [Figure 12 (d)].

Going back to the definitions of the paramenters entering the equation that governs the dislocation mobility [Equations (1) and (2)]; the effective Peierls stress (τ_0), Equation (2), is defined as the applied stress for which the nucleation free energy for a kink pair (ΔG) is zero. ΔG is given by:

$$\Delta G = E^{kink} \pm \tau l_P b L^{kink}, \tag{15}$$

where L^{kink} is the effective kink pair nucleation length and l_P is distance advanced by the dislocations; in the kinks studied here $l_P = |1/3a < 112 > |$. The second term in the right hand side of
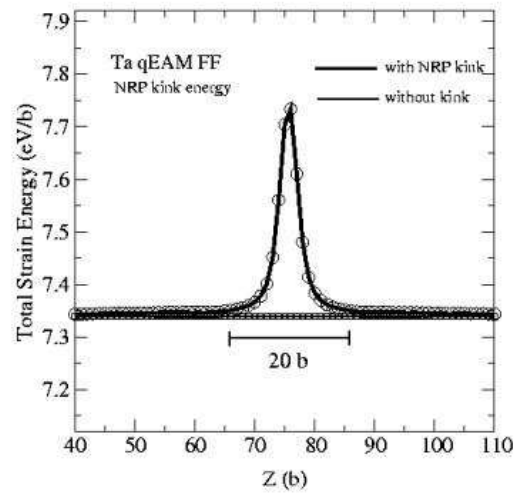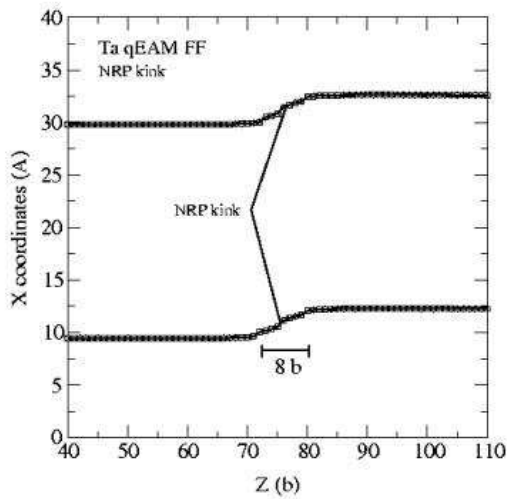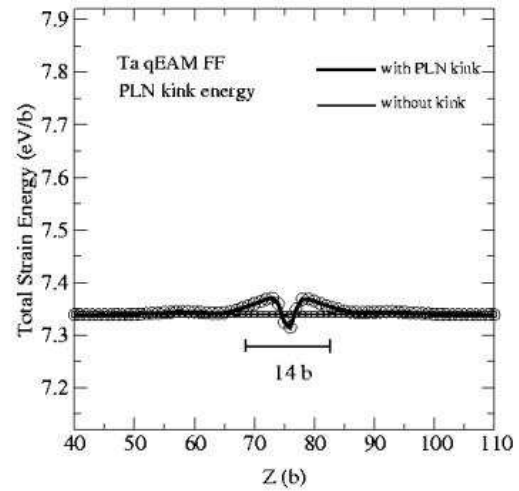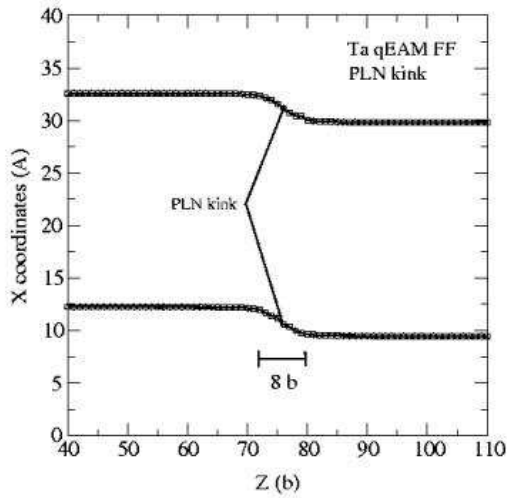
Figure 12: PLN and NRP kinks in Ta using the qEAM FF. (Top Left) PLN kink: Dislocation position in the [11-2] direction along the dislocation line; we can see the dislocation moves from one equilibrium position to the next in a distance of 10 Burgers vectors. (Top Right) PLN kink: total energy in the quadrupolar system with four PLN kinks along the dislocation line. The system is divided in slices with thickness equal to b and the energy in each region is calculated. (Bottom Left) NRP kink: Dislocation position in the [11-2] direction along the dislocation line; we can see the dislocation moves from one equilibrium position to the next in a distance of 10 Burgers vectors. (Bottom Right) NRP kink: total energy in the quadrupolar system with four PLN kinks along the dislocation line.
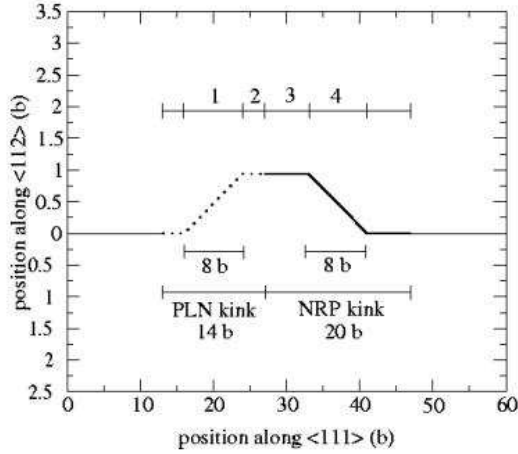
Figure 13: Schematic diagram of a kink pair formed by a NRP and PLN single kinks. The four terms entering in the work expresion (Equation 16) are shown in the Figure.

Equation 15 is the work done by the external stress when the kink is nucleated. Figure 13 shows a schematic diagram of a PLN-NRP kink pair. We can see that the work done by the external stress to nucleate the kink pair can be divided in four terms:

$$\tau b l_P L^{kink} = \tau b l_P \left(\frac{L_{str}^{PLN}}{2} + \frac{L_{ene}^{PLN} - L_{str}^{PLN}}{2} + \frac{L_{ene}^{NRP} - L_{str}^{NRP}}{2} + \frac{L_{str}^{NRP}}{2} \right) \qquad (16)$$

where L^{kink} is the effective kink pair length. In Figure 13 we show the four terms in the right hand side of Equation (16). Note that Equation 16 assumes that the kinks are straight lines connecting the two equilibrium positions of the dislocation. In this way we obtain the effective kink pair nucleation length $L^{kink} = 17$ b.

The remaining materials parameter is the nucleation energy of a jog E^{jog}. In this work we take E^{jog} as the PLN-NRP kink pair nucleation energy.

4   Experiment, Validation and Prediction

To test the predictive capabilities of the multiscale approach we first select a set of material parameters to best fit the experimental results, then we compare these parameters against the atomistically computed ones and finally we *predict* the macroscopic response using the atomistics parameters. As we shall see, the agreement between the *fitted* and *computed by atomistics* material parameters is remarkable, and the macroscopic predicted response retains most of the experimental features. These facts provide confidence in the multiscale modeling approach, indicating that even in the case that experimental data would not have been available, still the macroscopic behavior could have been predicted based only on atomistic calculations.

The experiment data correspond to uniaxial tests on Ta single crystals of Mitchell and Spitzig [47]. In these tests, 99.97%-pure Ta specimens were loaded in tension along the [213] crystallographic axis, at various combinations of temperature and strain rate. In particular we considered

Table 2: Material parameters for Tantalum

Parameter	Fitted set	Atomistic set	Units
E^{kink}	0.70	0.725	[eV]
L^{kink}/b	13	17	
$U^{\text{edge}}/\mu b^2$ (*)	0.2	0.216	
$U^{\text{edge}}/U^{\text{screw}}$	1.77**	1.77	
$\bar{l}/b$	5	5	
L^{junct}/b	20	20	
E^{cross}	0.67	.725	[eV]
λ_{FR}	2.3	4.5***	
κ_c/b	1250	500***	

* $\mu = \frac{3}{5}C_{44} + \frac{1}{5}(C_{11} - C_{12})$.

** Taken from the atomistic simulations.

*** Not computed by atomistics.

temperatures ranging from 296 K to 573 K, and strain rates ranging from 10^{-1} s^{-1} to 10^{-5} s^{-1}. The numerical procedure employed for the integration of the constitutive equations has been described elsewhere [48]. The constitutive update is fully implicit, with the active systems determined iteratively so as to minimize an incremental work function. All stress-strain curves are reported in terms of nominal stress and engineering strain.

Two different sets of material properties were used for the numerical simulations. The first set was obtained by fitting the simulation results to the experimental results. Table 2 identifies the subset of parameters which are also amenable to direct calculation by atomistic based methods. The table lists the parameter values obtained by these methods, as described in the previous sections, in parallel with the values obtained by the fitting approach. Thus, in the second set of properties which was used for numerical simulations, atomistic-based values replace fit-based values, when available. This is the case for the edge and screw dislocation self-energies, as well as the kink-pair formation energy and length. Clearly, those two sets don't differ by much, which strongly support the validity of the advertised multiscale paradigm. For a complete list of parameters for the model, the reader should refer to [7].

Figs. 14 and 15 show the predicted and measured stress-strain curves for a [213] Ta crystal over a range of temperatures and strain rates. One can compare, from top to bottom: the experimental results, the results obtained after fitting the parameters, and the results obtained with atomistic-based parameters. It is evident from these figures that the model, with both sets of parameters, captures salient features of the behavior of Ta crystals such as: the dependence of the initial yield point on temperature and strain rate; the presence of a marked stage I of easy glide, specially at low temperature and high strain rates; the sharp onset of stage II hardening and its tendency to shift towards lower strains, and eventually disappear, as the temperature increases or the strain rate increases; the parabolic stage II hardening at low strain rates or high temperatures; the stage II softening at high strain rates or low temperatures; the trend towards saturation at high strains; and
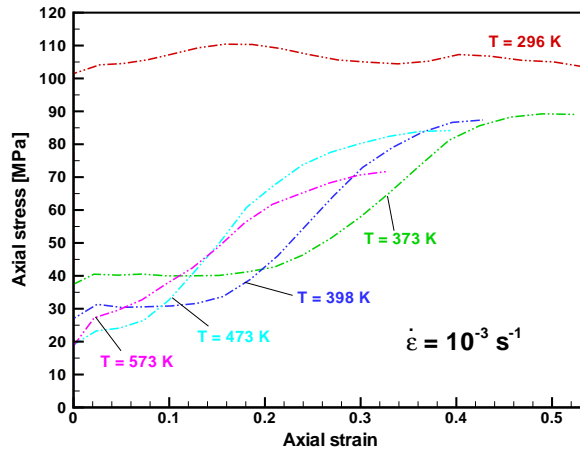
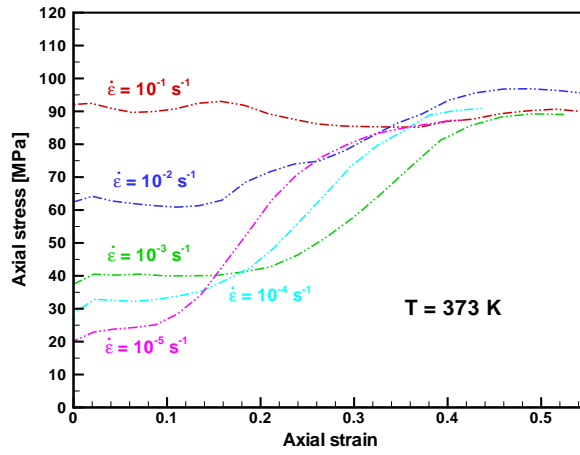(a) Experimental data of Mitchell & Spitzig [47]
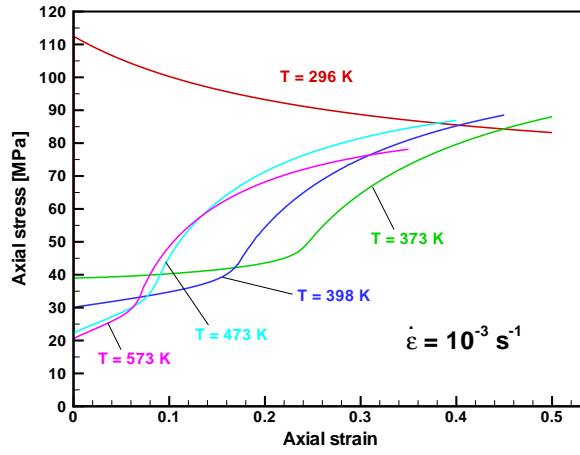
(b) Predictions of the model with fitted parameters
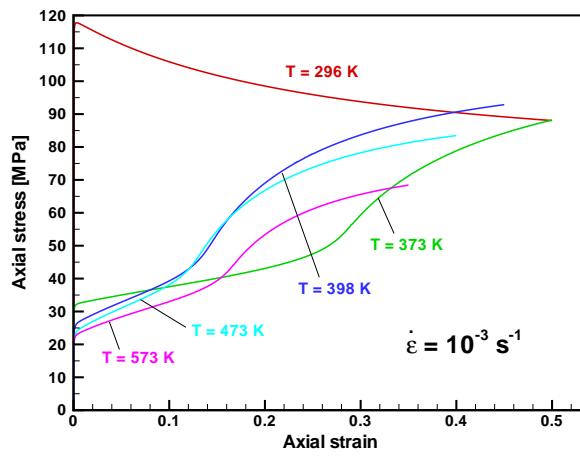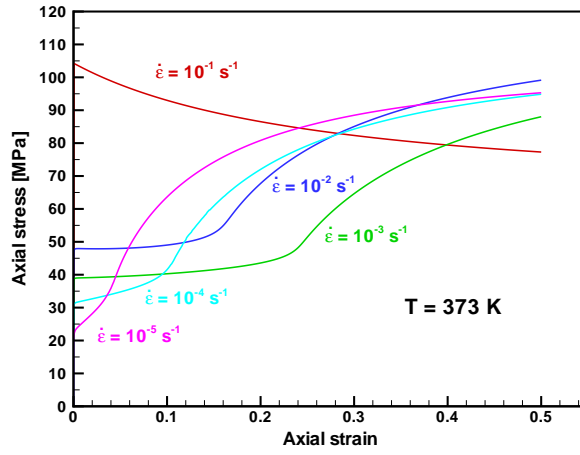

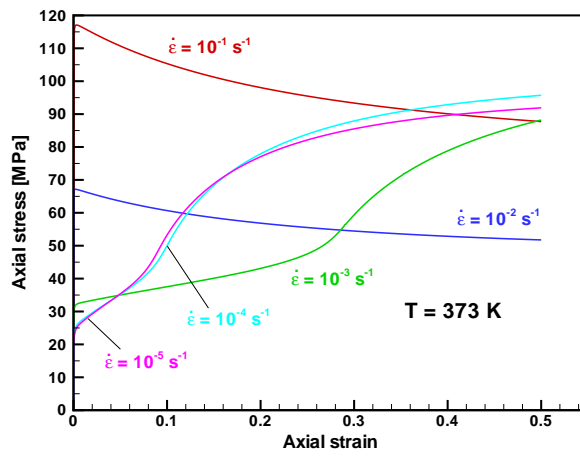(c) Predictions of the model with atomistic parameters

Figure 14: Temperature dependence of stress-strain curves for [213] Ta single crystal ($\dot{\epsilon} = 10^{-3}$ s^{-1}).

20

(a) Experimental data of Mitchell & Spitzig [47]

(b) Predictions of the model with fitted parameters

(c) Predictions of the model with atomistic parameters

Figure 15: Strain-rate dependence of stress-strain curves for [213] Ta single crystal (T=373 K).

the temperature and strain-rate dependence of the saturation stress. Thus, the predictive approach based on atomistic methods clearly shows its capacity to produce results matching the experimental evidence.

The theory reveals useful insights into the mechanisms underlying these behaviors. For instance, since during state I the crystal deforms in single slip and the secondary dislocation densities are low, the Peierls resistance dominates and the temperature and strain-rate dependency of yield owes mainly to the thermally activated formation of kinks and crossing of forest dislocations. It is interesting to note that during this stage the effect of increasing (decreasing) temperature is similar to the effect of decreasing (increasing) strain rate, as noted by Tang *et al.* [24]. The onset of stage II is due to the activation of secondary systems. The rate at which these secondary systems harden during stage I depends on the rate of dislocation multiplication in the primary system. This rate is in turn sensitive to the saturation strain γ^{sat}, which increases with strain rate and decreases with temperature. As a result, the length of the stage I of hardening is predicted to increase with strain rate and decrease with temperature, as observed experimentally. Finally, the saturation stress is mainly governed by the forest hardening mechanism and, in particular, by the strength of the forest obstacles. This process is less thermally activated than the Peierls stress, since the corresponding energy barriers are comparatively higher. Consequently, the stress-strain curves tend to converge in this regime, in keeping with observation.

The apparent softening observed in simulation results at the lowest temperature ($296\ K$) and the highest strain rate ($10^{-1}\ s^{-1}$) is actually an effect of the boundary conditions, allowing some level of rotation of the specimen. Since in those cases, the material hardening is relatively low (stage I only), this geometrical softening dominates in the apparent macroscopic behavior. In the other cases, the activation of several systems at high strains results in a more isotropic deformation, in turn leading to limited rotations. In order to take the exact experimental boundary conditions into account, a finite element model of the whole specimen should be used, allowing for a non-homogeneous deformation field.

Acknowledgments

References

[1] V.V. Bulatov and L.P. Kubin. Dislocation modelling at atomistic and mesoscopic scales. *Current Opinion in Solid State & Materials Science*, 3(6):558–561, 1998.

[2] R. Phillips. Multiscale modeling in the mechanics of materials. *Current Opinion in Solid State & Materials Science*, 3(6):526–532, 1998.

[3] G.H. Campbell, S.M. Foiles, H.C. Huang, D.A. Hughes, W.E. King, D.H. Lassila, D.J. Nikkel, T.D. de la Rubia, J.Y. Shu, and V.P. Smyshlyaev. Multi-scale modeling of polycrys-

tal plasticity: a workshop report. *Materials Science and Engineering A-Structural Materials Properties Microstructure and Processing*, 251(1-2):1–22, 1998.

[4] R. Phillips, D. Rodney, V. Shenoy, E. Tadmor, and M. Ortiz. Hierarchical models of plasticity: dislocation nucleation and interaction. *Modelling and Simulation in Materials Science and Engineering*, 7(5):769–780, 1999.

[5] J.A. Moriarty, W. Xu, P. Soderlind, J. Belak, L.H. Yang, and J. Zhu. Atomistic simulations for multiscale modeling in bcc metals. *Journal of Engineering Materials and Technology-Transactions of the ASME*, 121(2):120–125, 1999.

[6] M.I. Baskes. The status role of modeling and simulation in materials science and engineering. *Current Opinion in Solid State & Materials Science*, 4(3):273–277, 1999.

[7] A. M Cuitiño L. Stainer and M. Ortiz. Micromechanical modeling of hardening, rate sensitivity and thermal softening in bcc single crystals. *Journal of the Mechanics and Physics of Solids*, 2001.

[8] Duesbery, V. Vitek, and Bowen. *Proceedings of the Royal Society of London*, A332:85, 1973.

[9] V. Vitek. *Proceedings of the Royal Society of London*, A352:109, 1976.

[10] V. Vitek. Structure of dislocation cores in metallic materials and its impact on their plastic behavior. *Progress in Material Science*, 36:1–27, 1992.

[11] W. Xu and J.A. Moriarty. Atomistic simulation of ideal shear strength, point defects, and screw dislocations in bcc transition metals: Mo as a prototype. *Physical Review B-Condensed Matter*, 54(10):6941–6951, 1996.

[12] M.S. Duesbery and V. Vitek. Plastic anisotropy in bcc transition metals. *Acta Materialia*, 46(5):1481–1492, 1998.

[13] S. Ismail-Beigi and T.A. Arias. Ab initio study of screw dislocations in mo and ta: A new picture of plasticity in bcc transition metals. *Physical Review Letters*, 84(7):1499–1502, 2000.

[14] G. Wang, A. Strachan, T. Cagin, and W.A. III Goddard. Molecular dynamics simulations of 1/2a¡111¿ screw dislocation in ta. *Materials Science and Engineering A*, 2001.

[15] M.S. Duesbery and W. Xu. The motion of edge dislocations in body-centered cubic metals. *Scripta Materialia*, 39(3):283–287, 1998.

[16] P. B. Hirsch. In *5th International Conference on Crystallography*, page 139. Cambridge University, 1960.

[17] A. Seeger and P. Schiller. *Acta Metallurgica*, 10:348, 1962.

[18] J. P. Hirth and J. Lothe. *Theory of Dislocations*. McGraw-Hill, New York, 1968.

[19] J.P. Hirth and R.G. Hoagland. Nonlinearities in the static energetics and in the kinematics of dislocations. *Physica D*, 66(1-2):71–77, 1993.

[20] W. Xu and J.A. Moriarty. Accurate atomistic simulations of the peierls barrier and kink-pair formation energy for ¡ 111 ¿ screw dislocations in bcc mo. *Computational Materials Science*, 9(3-4):348–356, 1998.

[21] A. Seeger and L. Hollang. The flow-stress asymmetry of ultra-pure molybdenum single crystals. *Materials Transactions JIM*, 41(1):141–151, 2000.

[22] W. Wasserbäch. *Philosophical Magazine*, A53:335, 1986.

[23] R. Lachenmann and H. Schultz. *Scripta Metallurgica*, 4:33, 1970.

[24] M. Tang, B. Devincre, and L.P. Kubin. Simulation and modelling of forest hardening in body centre cubic crystals at low temperature. *Modelling and Simulation in Materials Science and Engineering*, 7(5):893–908, 1999.

[25] T. Suzuki, S. Takeuchi, and H. Yoshinaga. *Dislocation Dynamics and Plasticity*. Springer-Verlag, 1991.

[26] A.D. Brailsford. Electronic component of dislocation drag in metals. *Physical Review*, 186:959–961, 1969.

[27] M.I. Baskes, R.G. Hoagland, and T. Tsuji. An atomistic study of the strength of an extended-dislocation barrier. *Modelling and Simulation in Materials Science and Engineering*, 6(1):9–18, 1998.

[28] D. Rodney and R. Phillips. Structure and strength of dislocation junctions: An atomic level analysis. *Physical Review Letters*, 82(8):1704–1707, 1999.

[29] V.B. Shenoy, R.V. Kukta, and R. Phillips. Mesoscopic analysis of structure and strength of dislocation junctions in fcc metals. *Physical Review Letters*, 84(7):1491–1494, 2000.

[30] G. Danna and W. Benoit. Dynamic recovery of the microstructure of screw dislocations in high-purity bcc metals. *Materials Science and Engineering A-Structural Materials Properties Microstructure and Processing*, 164(1-2):191–195, 1993.

[31] M. Rhee, H.M. Zbib, J.P. Hirth, H. Huang, and T. de la Rubia. Models for long-/short-range interactions and cross slip in 3d dislocation simulation of bcc single crystals. *Modelling and Simulation in Materials Science and Engineering*, 6(4):467–492, 1998.

[32] H.C. Huang, N. Ghoniem, T.D. de la Rubia, M. Rhee, H. Zbib, and J. Hirth. Stability of dislocation short-range reactions in bcc crystals. *Journal of Engineering Materials and Technology- Transactions of the ASME*, 121(2):143–150, 1999.

[33] L. P. Kubin, B. Devincre, and M. Tang. *Journal of Computer Aided Material Design*, 5:31, 1998.

[34] H.M. Zbib, T.D. de la Rubia, M. Rhee, and J.P. Hirth. 3d dislocation dynamics: stress-strain behavior and hardening mechanisms in fcc and bcc metals. *Journal of Nuclear Materials*, 276:154–165, 2000.

[35] P. Franciosi and A. Zaoui. Multislip in f.c.c. crystals: A theoretical approach compared with experimental data. *Acta Metallurgica*, 30:1627, 1982.

[36] P. Franciosi and A. Zaoui. Glide mechanisms in b.c.c. crystals: an investigation of the case of α-iron through multislip and latent hardening tests. *Acta Metallurgica*, 31:1331, 1983.

[37] D. Kuhlmann-Wilsdorf. Theory of plastic deformation: properties of low energy dislocation structures. *Materials Science and Engineering*, A113:1, 1989.

[38] W. G. Johnston and J. J. Gilman. Dislocation velocities, dislocation densities and plastic flow in lithium fluoride crystals. *Journal of Applied Physics*, 30:129, 1959.

[39] W. G. Johnston and J. J. Gilman. Dislocation multiplication in lithium fluoride crystals. *Journal of Applied Physics*, 31:632, 1960.

[40] P. P. Gillis and J. Gilman. Dynamical Dislocation Theory of Crystal Plasticity. II. Easy Glide and Strain Hardening. *Journal of Applied Physics*, 36:3380, 1965.

[41] U. Essmann and M. Rapp. Slip in copper crystals following weak neutron bombardment. *Acta Metallurgica*, 21:1305, 1973.

[42] K.P.D. Lagerlof. On deformation twinning in bcc metals. *Acta Metallurgica et Materialia*, 41(7):2143–2151, 1993.

[43] H. Dybiec. Model of the early deformation stage of bcc metals in low-temperature. *Zeitschrift für Metallkunde*, 86(7):512–517, 1995.

[44] Oguz Gulseren Sonali Mukherjee R. E. Cohen Alejandro Strachan, Tahir Cagin and William A. Goddard III. First principles force field for metallic tantalum. *Physical Review B*, 2001.

[45] Tahir Cagin Alejandro Strachan and William A. Goddard III. Critical behavior in spallation failure of metals. *Physical Review B*, 63:0601034, 2001.

[46] Tahir Cagin Guofeng Wang, Alejandro Strachan and William A. Goddard III. Kinks in a/2¡111¿ screw dislocation in ta. *Journal of Computer Aided Materials Design*, 2001.

[47] T.E. Mitchell and W.A. Spitzig. Three-stage hardening in tantalum single crystals. *Acta Metallurgica*, 13:1169–1179, 1965.

[48] M. Ortiz and L. Stainier. The variational formulation of viscoplastic constitutive updates. *Computer Methods in Applied Mechanics and Engineering*, 171(3-4):419–444, 1999.